Modularized Paper Actuator Based on Shape Memory Alloy, Printed Heater, and Origami

Ke Zheng, Enlai Gao, Bin Tian, Jing Liang, Qun Liu, Enbo Xue, Qian Shao,* and Wei Wu*

Smart materials promote the development of soft actuators. Herein, the modularized origami soft actuators consisting of shape memory alloy (SMA) wires, foldable paper-based heaters, and paper substrates with special origami structures are proposed, which are connected without adhesive and allow convenient replacement for damaged parts. SMA wires are threaded into the paper as a drive module. The foldable paper-based heaters with a length of 288 mm can be heated to 105.1 °C at 6.5 V to control the origami soft actuators. Combined with theoretical calculations and experimental measurements, the origami structure is adopted which exhibits a high recoverability compared with the flat structure because the design finds a structure–material balance by increasing structural flexural rigidity (2 times of that flat structure) for improving the restoring force while maintaining the deformation of materials within the elastic region during the actuation. The three modules in the origami actuator are independent and perform their functions individually. The combined system can also become a module that provides a driving force in other devices. This work provides a novel route and insight for developing modular soft actuators.

1. Introduction

Soft actuators with high adaptability in complex environments are attractive for applications in soft grippers, artificial muscles, wearables, haptic devices, and medical devices.[1–3] In general, smart actuator materials and device design play the key role for the function of soft actuators.[4–12] Therefore, many kinds of conventional smart materials including humidity-responsive materials, light-responsive polymers, shape memory polymers, and shape memory alloys (SMAs) are studied and used for developing miniaturized and intelligent soft actuators.[13–16] Among in those smart response actuators, humidity-actuated soft actuators are often built by a multilayer architecture capable of functional actuation.[17,18] However, it has some problems such as interlayer shedding. The manufacture of soft actuators composed of polymer requires complex synthesis processes of monomer polymer and polymerization conditions.[19] SMAs are driven by the phase transformation of martensite and austenite, and do not require a complex multilayer structure and complex synthesis processes.[20] In addition, SMAs have many advantages such as high-energy density, excellent biocompatibility, and long service life, showing great potential in practical applications.[21] Once the crystalline phase transition occurs, it is difficult for the unidirectional SMA wire to return to its initial set shape without applying any external force. Thus, it is common to embed unidirectional SMA into the polymer matrix or custom framework, which provides the driving force to the soft actuator.[22–24] This embedded structure design can achieve good driving performance, but it is difficult to achieve targeted replacement of damaged parts, resulting in a short service life of actuator and waste of materials.

Cellulose paper has outstanding advantages such as low cost, degradable, renewable, environmentally friendly, and malleable, and is a promising candidate for combining with SMA for sustainable soft actuators.[25,26] The pristine flat structure of paper limits the application scenarios because its insufficient recoverability upon deformation cannot satisfy the need of soft actuators. Origami, as a powerful technique, can transform 2D sheet into 3D structure with fantastic and controllable mechanical behaviors.[27–29] However, designing suitable 3D structures to meet deformation recovery requirements remains a challenge. On the other hand, the power supplying for the actuator system (combination of paper and SMAs) is also an essential part and needs to be considered carefully. In our previous works, we developed flexible heaters to apply in the thermochromic displays, defogging for windows, and wearable thermotherapy.[30,31]

K. Zheng, B. Tian, J. Liang, Q. Liu, E. Xue, W. Wu
Laboratory of Printable Functional Materials and Printed Electronics
Research Center for Graphic Communication, Printing and Packaging
Wuhan University
Wuhan 430072, P. R. China
E-mail: weiwu@whu.edu.cn

E. Gao, Q. Shao
Department of Engineering Mechanics
School of Civil Engineering
Wuhan University
Wuhan 430072, P. R. China
E-mail: qian.shao@whu.edu.cn

The ORCID identification number(s) for the author(s) of this article can be found under https://doi.org/10.1002/aisy.202200194.

If we introduce the flexible heater into the proposed actuator system, it could serve as an effective driving module for SMAs.

Herein, we first propose a new method without glue for the fabrication of origami soft actuator (OSA). This OSA consists of three units: SMA wires that generate the actuating force, printed heaters for the thermal stimulation, and elastic origami structures that provide recovery force. To facilitate targeted replacement, the OSA is free of any adhesive connection. SMA wires are threaded into the origami structure, and the paper-based heaters are completely wrapped around the SMA wires, which is tightly attached to the origami structure using a plug-in method. Origami structures as an infrastructure enable continuous actuation. Finite element simulations demonstrated that the flexural rigidity of origami structure is increased by approximately 2 times of that for the flat structure. Printed heaters with the length of 288 mm can provide stable actuation temperatures of 105.1 °C under the applied voltage of 6.5 V. The SMA wires induce structural movements upon the thermal stimulus. Conversely, in the absence of thermal stimulation, the origami structure generates a restoring force that drives the SMA wire back to its initial state.

2. Results and Discussion

Figure 1 demonstrates the components of the OSA and the actuation process. First, the patterned heater based on silver fractal dendrites (Ag FDs) is fabricated by screen printing method and then folded into a predesired shape. Then, SMA wires can change shape freely at room temperature. Finally, the prepunched craft paper is folded according to the crease line to obtain the origami structure. As shown in Figure S1 (Supporting Information), each unit is independent on each other, and any element is convenient to replace without affecting other units. The actuator is achieved by assembling these units together. The X-ray diffraction (XRD) pattern and scanning electron microscopy (SEM) image of Ag FDs are shown in Figure S2 (Supporting Information). The diffraction peaks of Ag FDs are consistent with the pure Ag (JCPDS card no. 04-0783) and the

Ag FDs show uniform fractal dendrites nanostructures, revealing the successful synthesis of Ag FDs.

To obtain the optimal actuation performance of the OSA, the experimental temperature range of the heaters is investigated. According to the differential scanning calorimetry (DSC) characterization, the austenite finish (A_f) and martensitic finish (M_f) temperature of SMA wires is 72.0 and 49.7 °C, respectively (**Figure 2**a). The SMA wires can change shape from curved to straight when the temperature is higher than A_f. As a result, the lowest actuation temperature of OSA is 72.0 °C. Accordingly, the bending angle of SMA wires as a function of temperature is tested. As shown in Figure 2b, the bending angle is defined as a tangent degree at the end of the wires, and the time of its change is served as a temperature-sensitive criterion. A single SMA wire is bent into a circle before heating, and then placed on a heating platform. The inset of Figure 2b shows the configurations of a SMA wire during the heating process at 100 °C. As the temperature increases, the time required for the same change in the bending angle of the SMA wire reduces. The time required for the shapes changing from curved to flat is 26, 9, 6, 4, and 4 s at 80, 90, 100, 110, and 120 °C, respectively. Obviously, the response time of SMA wire at 100 °C is about 4.3 times shorter than that at 80 °C and is nearly equal to those at 110 and 120 °C. When the temperature exceeds 100 °C, the mechanical properties of the cellulose paper will decrease, thereby affecting the life of the device. Therefore, when the time is relatively close, 100 °C is selected as the test temperature for subsequent experiment.

To achieve good driving effect of the actuator, a flexible heater is introduced and fabricated by screen printing method. Conductive ink is made of Ag FDs as conductive material and polystyrene-block-polyisoprene-block-polystyrene (SIS) as binder. The resistive-type heater is an efficient device for converting electric energy into heat energy, mainly resulting from Joule heat effect,

$$P = \frac{U^2}{R} = UI \tag{1}$$

where P is the electrical power, U is the applied voltage, R is the electrical resistance, and I is the current through the heater. When controlling the voltage, the resistance becomes the main factor
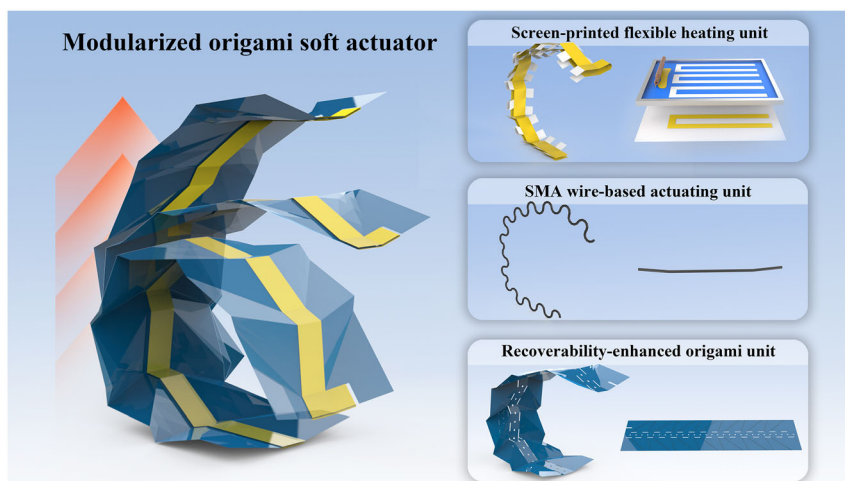

Figure 1. Schematic diagram of manufacturing, component units, and actuation of the OSA.
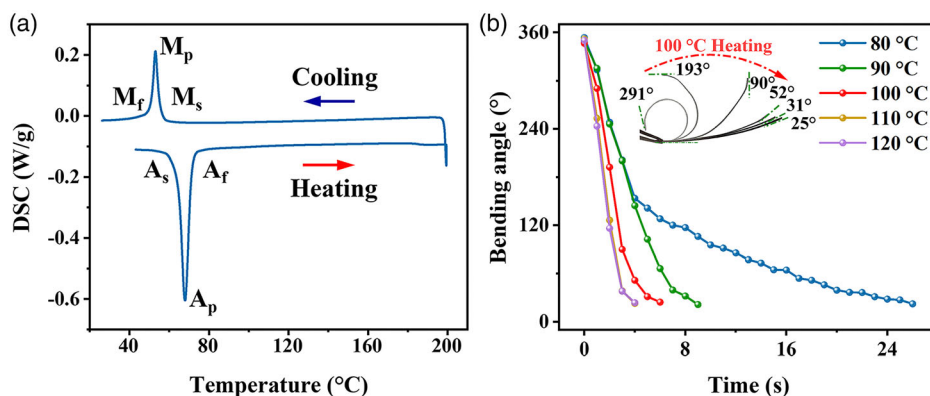
Figure 2. a) DSC measurement of SMA wires. b) The change of bending angle of SMA wires at 80, 90, 100, 110, and 120 °C, respectively. The change of bending configuration at 100 °C is shown in an inset image.

affecting the thermal stimulus. But the resistance of flexible heater is usually difficult to control. Screen printing technology is an excellent tool to address this issue by controlling the number of printing layers, and thus realizes the free control of temperature. **Figure 3**a reveals the sheet resistance of the printed heaters on 80 g m^{-2} copy paper, 150 and 300 g m^{-2} craft paper (H-80CoP, H-150CrP, and H-300CrP) with two to five layers, respectively. The sheet resistance of heaters is gradually decreased as the number of printed layers increases. Among the three paper substrates with different weights, H-80CoP delivers a relatively lower sheet resistance at the same printed layers. The Joule heating effect of these printed heaters is further investigated. The saturation temperatures are compared among different printed layers and different weights of paper substrates when a constant voltage of 0.4, 0.6, 0.8, and 1 V is applied (Figure S3 in Supporting Information and Figure 3b). When the applied voltage is 1 V, the saturation temperatures that can be reached by H-80CoP with 3 layers, H-150CrP with 4 layers, and H-300CrP with 5 layers (denoted as H-80CoP-3L, H-150CrP-4L, and H-300CrP-5L, respectively) are 98.3, 96.1, and 95.3 °C, respectively. The temperature is not significantly increased as the increasing of printed layers. Therefore, considering the low cost, the H-80CoP-3L is the promising and optimizing substrate to satisfy the application demand.

Because of the mechanical properties of flexible heaters are important in OSA applications, we investigated the changes in electrical resistance of paper-based heaters under cyclic mechanical loading. Three types of heaters are tested: H-80CoP-3L, H-150CrP-4L, and H-300CrP-5L. The three heaters are continuously folded by 100 times and the changes in resistance are recorded. The value of R/R_0 is measured for the comparison of the fold resistance, where R_0 is the initial resistance and R is the resistance after folding. As shown in Figure 3d, the resistance of H-80CoP-3L remained stable and only increased by 1.23 times after 100 folds. The resistance of other two heaters is increased diversely when folded 100 times. The resistance of H-150CrP-4L and H-300CrP-5L becomes 9.08 and 23.83 times higher than the initial values, respectively. In order to better understand the effect of folding on the heater, the bending strain is calculated. According to the formula of bending strain

$$\varepsilon = \frac{h}{2r} \tag{2}$$

where ε is the bending strain, h is the sample thickness, and r is the bending radius.[32] The bending radius can be calculated as follows

$$r = \frac{L_{\mathrm{initial}}}{2\pi \sqrt{\dfrac{\Delta L}{L_{\mathrm{initial}}} - \dfrac{\pi^2 h^2}{12 L_{\mathrm{initial}}^2}}} \tag{3}$$

where L_{initial} is the initial clamping length of heater; ΔL is the value of change in clamping length during bending.[33] As shown in Table S1 (Supporting Information), the L_{initial} and ΔL of the three heaters are equal, although the heaters have different h value, according to this formula, it does not affect their r to be nearly equal. Therefore, the bending strains are mainly related to the h value. According to the calculation, the bending strains of H-80CoP-3L, H-150CrP-4L, and H-300CrP-5L are 1.4%, 2.6%, and 4.9%, respectively. Obviously, when the bending radius is fixed, the larger the device thickness leads to the larger the bending strain, the greater the damage to the heater is. As shown in Figure S4 (Supporting Information), the folded positions of the three heaters are investigated by SEM. The H-80CoP-3L has no obvious change in microstructure after 100 folding-releasing cycles, while the H-150CrP-4L and H-300CrP-5L appear different degrees of cracks (Figure S4 in Supporting Information). Subsequently, different voltages of 0.4, 0.6, 0.8, and 1 V are applied to the three heaters that have been folded 100 times. As the voltage rises, the saturation temperature of the three heaters gradually increases (Figure 3e). When the voltage of 1 V is applied, the saturation temperatures of H-80CoP-3L, H-150CrP-4L, and H-300CrP-5L are 105.9, 89.4, and 80.4 °C, respectively, where H-80CoP-3L shows good thermal performance. As shown in Figure 3c,f, the heating performances before and after folding are captured by the IR camera. Folding reduces the uniformity and values of the saturation temperature of H-150CrP-4L and H-300CrP-5L, while displays negligible effect on the H-80CoP-3L heaters. Based on the
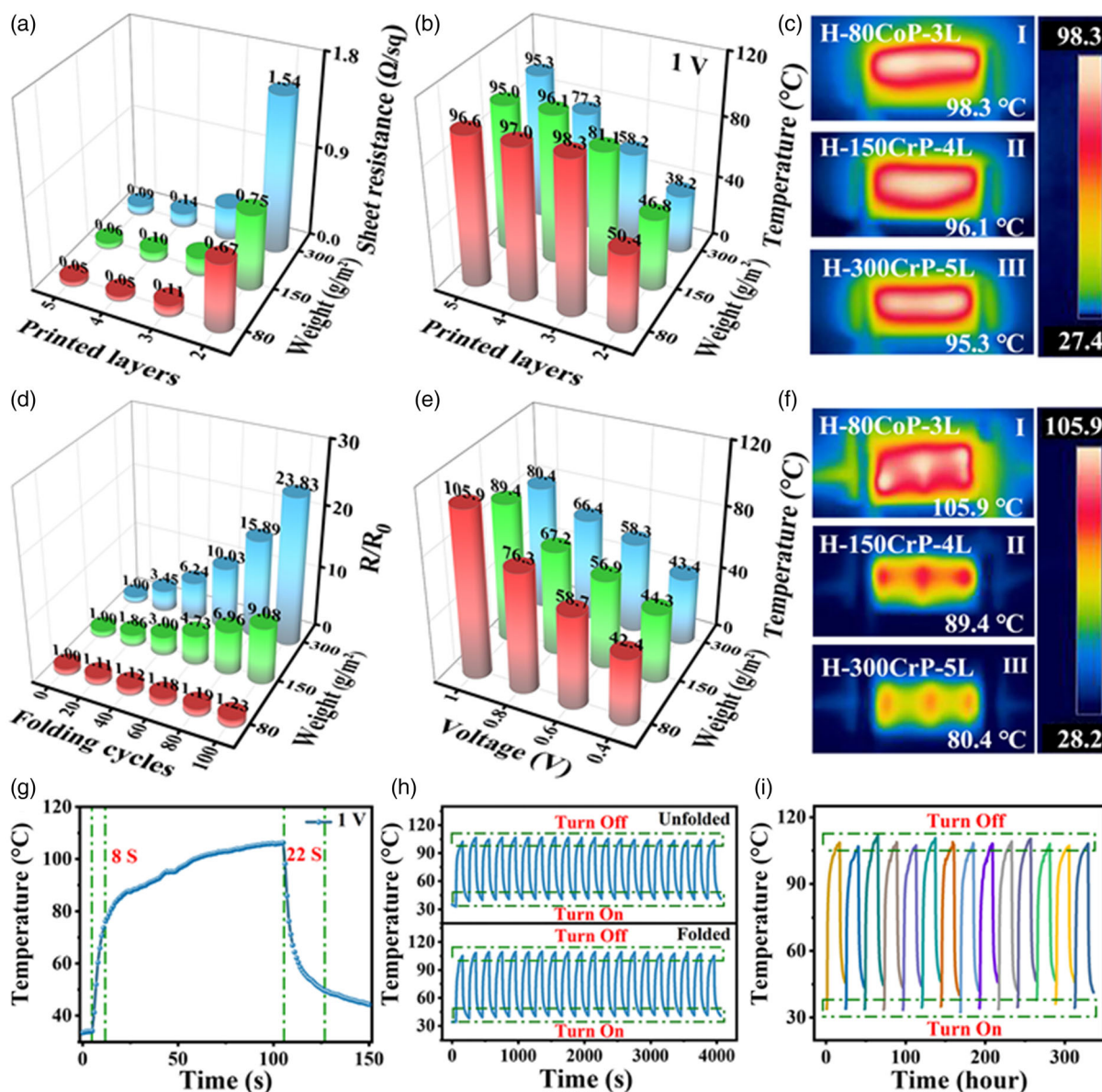
Figure 3. a,b) The sheet resistance and the temperature versus different printed layers (2, 3, 4, and 5 layers) on H-80CoP, H-150CrP, and H-300CrP, respectively. c) IR images of H-80CoP-3L, H-150CrP-4L, and H-300CrP-5L before folding. d) The change of resistance of H-80CoP-3L, H-150CrP-4L, and H-300CrP-5L in the process of folding 100 times continuously. e) The saturation temperature of H-80CoP-3L, H-150CrP-4L, and H-300CrP-5L samples with the testing voltage of 0.4, 0.6, 0.8, and 1 V, respectively. f) IR images of H-80CoP-3L, H-150CrP-4L, and H-300CrP-5L after folding. g) Response time of the folded H-80CoP-3L. h) Twenty heated cycles of the H-80CoP-3L. i) Stability test of the folded H-80CoP-3L. Note that the results of temperature testing and IR image are measured at the voltage of 1 V.

above results, H-80CoP-3L with excellent heating performance and foldability is used for further performance tests.

As the thermal response time and thermal stability are important indicators for evaluating the performance of heaters, the H-80CoP-3L heaters were tested in this work. As shown in Figure 3g, the folded H-80CoP-3L takes only 8 s to rise the heated temperature from 34.0 to 73.8 °C ($A_f = 72$ °C) when applied voltage is 1 V. It took 22 s to cool down from 106.2 to 49.5 °C ($M_f = 49.7$ °C) after power off. This result proves that the H-80CoP-3L heater possesses the fast thermal response and short cooling time. Figure 3h shows the 20 cyclic Joule heating

tests of the H-80CoP-3L heater before and after 100 times of folding at 1 V, demonstrating that the H-80CoP-3L heater possesses a stable cyclic heating performance without being affected by folding. Additionally, the heating performance of folded H-80CoP-3L at 1 V in ambient environment is monitored for 14 days (Figure 3i). The heating performance is excellent in air.

To satisfy the application demands of OSA, H-80CoP-3L solution is used to prepare the large heater (LH-80CoP-3L). As shown in **Figure 4**a (I, II), the LH-80CoP-3L with the length of 288 mm is folded in half for use. The middle part is used as a temperature measurement standard, and the data are recorded. The
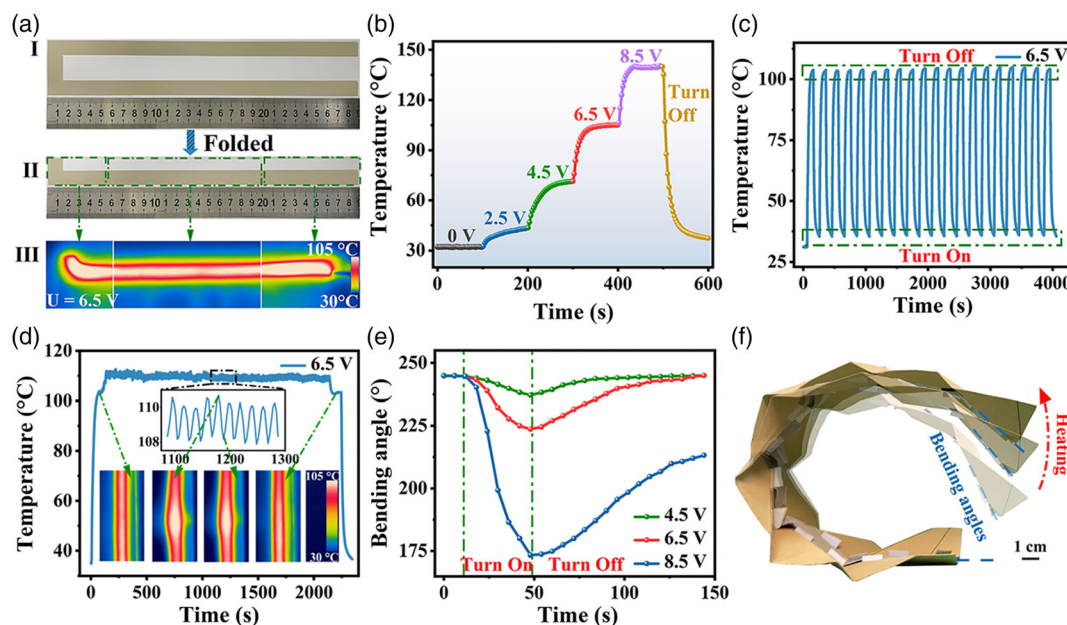
**ADVANCED
SCIENCE NEWS**

www.advancedsciencenews.com

**ADVANCED
INTELLIGENT
SYSTEMS**
Open Access

www.advintellsyst.com

Figure 4. a) I, II) The images of LH-80CoP-3L before and after folding. III) IR image of LH-80CoP-3L after folding when 6.5 V is applied. b) Transient temperature changed of the LH-80CoP-3L during the gradual rise of voltage from 0 to 2.5, 4.5, 6.5, and 8.5 V. c) Twenty heating cycles of the LH-80CoP-3L under 6.5 V. d) Temperature changed of LH-80CoP-3L with IR images during 100 times bending extension cycle test when the applied voltage is 6.5 V. e) The changes of OSA bending angle when applying 4.5, 6.5, and 8.5 V to the LH-80CoP-3L, respectively. f) OSA images taken during the heating.

LH-80CoP-3L exhibits an excellent Joule heating performance, which can be heated to 43.3, 71.2, 105.1, and 139.8 °C at 2.5, 4.5, 6.5, and 8.5 V, respectively (Figure 4b). Providing a voltage of 6.5 V can make the heater reach about 100 °C, so 6.5 V is set as the control voltage. Figure 4a-III shows the uniform temperature distribution of the LH-80CoP-3L when a voltage of 6.5 V is applied. Figure 4c shows the temperature variation of the LH-80CoP-3L under 20 cycles Joule heating at the voltage of 6.5 V, demonstrating a stable cyclic heating performance of the LH-80CoP-3L. Time-dependent temperatures at various status are presented in Figure 4d together with the corresponding temperature distribution captured by IR camera shown as insets. To simulate the practical application environment, a stable 6.5 V voltage is supplied to LH-80CoP-3L. When the temperature is stabilized at about 103 °C, 100 times consecutive bending cycles are performed, during which the temperature always fluctuates at around 109 °C. After the cycle is stopped, the temperature of LH-80CoP-3L is returned to around 103 °C, confirming the excellent reliability. Furthermore, the relationship between voltage and the actuation effect of OSA is investigated (Figure 4e). The bending angles of the OSA are 237.1°, 223.7°, and 173.4° as using the applied voltage of 4.5, 6.5, and 8.5 V for 36 s, respectively. After turning off the applied voltage of 4.5 and 6.5 V, the OSA would be recovered and return to its initial state within 96 s. Obviously, the bending angle obtained at 6.5 V is more suitable for practical applications than that of 4.5 V. In contrast, an applied voltage of 6.5 V endows the OSA with the best heating performance than other samples. Figure 4f shows the cumulative images taken during the actuation process with the Joule heating method.

The mechanical behaviors and the recoverability of the actuators rolled up from different origami structures and flat paper structures are investigated by theoretical and numerical analyses. According to Euler–Bernoulli beam theory, the maximum tensile and compressive strains of the paper structures occur at the outmost surfaces during the bending actuation. Assuming the flat structures deforms from nearly a circle (with a diameter of $d = 100$ mm and a thickness of $t = 0.4$ mm) into a flat sheet, based on Euler–Bernoulli beam theory, the magnitude of the maximum strain is estimated as only $\approx t/(d + t) = 0.4\%$, which is much lower than the elastic strain limit of the paper sheets (on the order of $\approx 1.0\%$, **Figure 5**b). For the origami structures, the maximum strain is difficult to be estimated from the beam theory owing to its structural complexity. Thus, it is necessary to utilize finite element method (FEM) calculations to predict the strain distributions of them. Three origami structures having various inside and outside folding lengths (i.e., the ratios of the inside folding length to the outside folding length are 1:1, 1:3, and 1:5, respectively, Figure 5a) are designed, and their mechanical behaviors are analyzed numerically. As shown in Figure 5a, when these structures have the same vertical displacement of 60 mm at the free ends, all the maximum principal strains of the deformed structures are less than 1.0%. Thus, the deformed origami structures and flat structures are still within the elastic region and no plastic deformation occurs during actuation, indicating that all structures could completely recover if no other mechanical perturbations exist after unloading. However, considering mechanical perturbations on the actuators, for example, the Movie S1 (Supporting Information) shows the hysteresis and damping of the alloy wires attached onto these structures, the
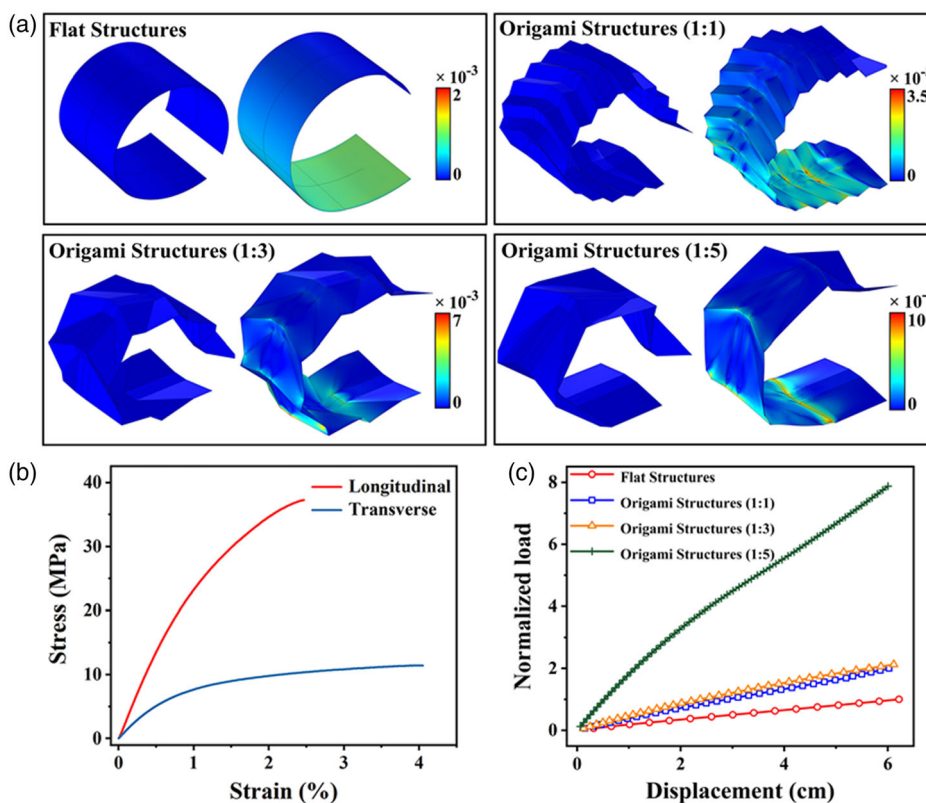
**ADVANCED
SCIENCE NEWS**

www.advancedsciencenews.com

**ADVANCED
INTELLIGENT
SYSTEMS**

www.advintellsyst.com

Figure 5. a) FEM predicted deformations of different paper structures, in which the color bars denote the distributions of maximum principal strains. b) Experimental tests of the stress and strain relationship in the longitudinal and transverse directions of paper sheets under uniaxial stress. c) FEM predicted vertical displacement of the top end of the different structures under different actuation steps. Note that the driving force is normalized using the maximum loading value applied to the flat structure.

mechanical resistance cannot be neglected in the actual situation. To overcome such resistance for improved recoverability of the actuators, the paper structure is required to supply a sufficient restoring force, which can be accomplished by increasing the flexural rigidity of paper structures. An estimation based on the beam theory indicates that the area moment of inertia for origami structures is ≈2 orders of magnitude higher than that for the flat structure, resulting in a significantly improved flexural rigidity ($D = E \times I$, where E is Young's modulus and I is the area moment of inertia of sheets) of origami structures. As an evidence, FEM calculations show that the apparent flexural rigidity for the 1:1 and 1:3 origami structures is approximately 2 times of that for flat structure, and that for the 1:5 origami structure is approximately 8 times (Figure 5c), falling within the theoretical estimation. On one hand, the significantly improved flexural rigidity benefiting from the origami structures would help to resist mechanical perturbations, and thus exhibit a high recoverability. On the other hand, a balance between the actuating load and the flexural rigidity should be considered. If the structure has a low flexural rigidity, it may not fully recover after unloading due to mechanical perturbations. While if the structure has a high flexural rigidity, a relatively high load is required to actuate its deformation. Several experimental tests show that the flexural rigidity of the flat structure is too low so that the structure cannot fully recover after unloading. The 1:1 and 1:3 origami structures can be actuated in a considerably

short time and their flexural rigidities are sufficient to provide a good recoverability. The 1:5 origami structure is so rigid that it is difficult to actuate its deformation. Therefore, in the mechanics point of view, the 1:1 and 1:3 origami structures are the optimal paper structures that balance the actuation performance and the recoverability. Considering that the 1:3 origami structure is simpler to be manufactured, we select this structure to assemble the actuator device.

Furthermore, FEM calculations are performed to investigate the recoverability of the FSA and OSA made of the 1:3 origami structure. As the temperature rises, the deformation of SMA wires leads to the lift of the free ends of soft actuators. Once the temperature starts to drop, the mechanical force results from the deformation of SMA wires reduces. And the flexural rigidity of paper structures, which resist their deformations, would trigger the actuators to recover from the deformed states. Meanwhile, inelastic deformations can occur in the SMA wires and the heaters, and result in a residual stress in the soft actuators, which is difficult to be estimated or tested experimentally. To study the influence of this residual stress on the recoverability of the soft actuators, without loss of generality, we assume that after unloading, a loading value of one-third of the normalized load remains on the structure and the same loading direction is kept. This load is applied on the deformed soft actuators and the recovery of both actuators is computed (**Figure 6**a,b). It is shown that at the same level of residual load, the OSA can almost fully

**ADVANCED
SCIENCE NEWS**

www.advancedsciencenews.com

**ADVANCED
INTELLIGENT
SYSTEMS**
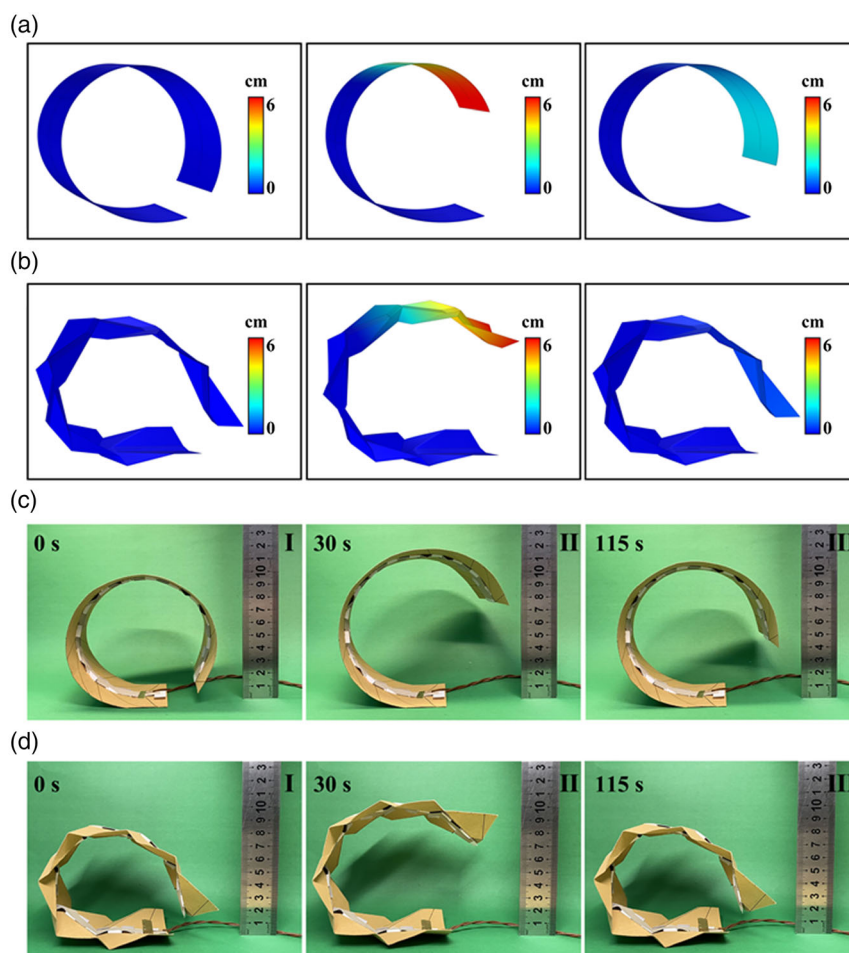Open Access

www.advintellsyst.com

Figure 6. a,b) FEM calculations and c,d) experimental verification of FSA and OSA recoverability comparison.

recover, while the FSA still has a vertical displacement of approximately 20 mm at the free end.

The recoverability of the soft actuators is also tested experimentally. FSA and OSA are fixed at one end and the free end is kept at an approximately equal initial height of about 15 mm (Figure 6c,d-I). The temperature of heater is controlled to reach about 100 °C, so that the free ends of the two soft actuators raise to a height of about 75 mm at 30 s (Figure 6c-II, d-II). After cooling for 85 s, the OSA can be restored to the initial position, while the FSA recovers to a height of about 45 mm and cannot be fully recovered (Figure 6c-III, d-III). The movie of recoverability comparison appears in Movie S2 (Supporting Information). The experimental results are consistent with the FEM calculations, demonstrating a significantly higher recoverability of the OSA than FSA. Hence, these results account for the improved recoverability and robust actuation of OSA as compared with that of FSA.

In order to further explore the practical application of OSA in multiple scenarios, the two OSAs serve as the wings of a-thousand-paper cranes that can swing when powered on, as shown in **Figure 7**a and Movie S3 (Supporting Information). The wings can be opened from bent shapes within 35 s when powered on, and then recover to its initial bending state after turning the power off for 105 s. Folding the ends of the paper into the designed shape can achieve the lifting function as shown in Figure 7b and Movie S4 (Supporting Information). Once powered on, the OSA can lift a 5.0 g clip within 60 s, and return to its initial state when powered off. As shown in Figure 7c and Movie S5 (Supporting Information), a single OSA relies on friction force to move objects. After the heater is turned on, the OSA contacts with the upper plane and generates a forward force to push the trolley to move. When the heater is turned off, the OSA is disconnected from the above plane and the trolley remains stationary. The trolley can move forward by turning the power to the heater on and off. A total forward distance of 43 mm is achieved in 418 s. The modularity of OSA is mainly reflected on three kinds of the smaller independent units that can be applied in other areas. Moreover, the OSA as a whole system to be a unit can be used as an important module in other devices.

3. Conclusions

In summary, we fabricated a modularized OSA, which is composed of origami structures, SMA wires, and screen-printed flexible heaters. In the elastic region, the paper sheet has a more
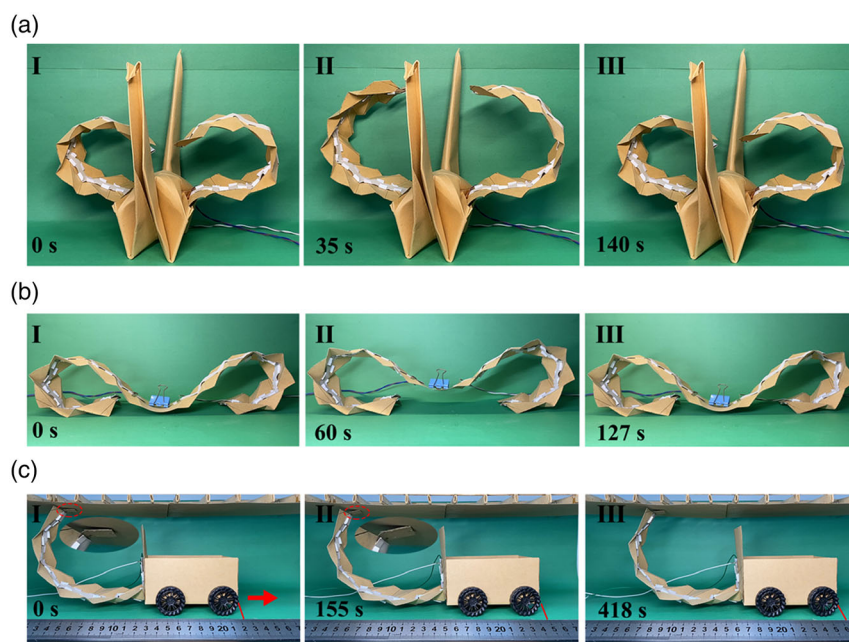
**ADVANCED
SCIENCE NEWS**

www.advancedsciencenews.com

**ADVANCED
INTELLIGENT
SYSTEMS**

www.advintellsyst.com

Figure 7. a) Two OSAs form the waving wings of a-thousand-paper cranes. b) Two OSAs work together to lift heavy objects. c) A single OSA can push a trolley.

stable bending structure and greater recoverability at folded status than unfolded status. Theoretical analyses and FEM calculations revealed the underlying mechanism behind the high recoverability of the origami structure, i.e., a structure–material balanced design by increasing the structural flexural rigidity while maintaining the material deformation within elasticity during the whole actuation. SMA wires exhibit high energy density and long life in the actuation process. LH-80CoP-3L with high heat production efficiency is screen printed by using Ag FDs conductive ink to achieve 105.1 °C at 6.5 V. Cellulose paper is readily available as the main material for OSA, while all of them are fixed by using a plug-in assembled, creating conditions for replacement. The concepts proposed in this work provide a paradigm for the development of modularized OSAs.

4. Experimental Section

Materials: Silver nitrate (AgNO₃, AR) and xylene (C₈H₁₀, AR) were bought from Sinopharm Chemical Reagent Co., Ltd. Hydroxylamine solution (H₃NO, 50 wt% in H₂O) and polystyrene–*block*-polyisoprene–*block*-polystyrene (SIS) were purchased from Sigma-Aldrich Co., Ltd. Deionized water (18.2 MΩ) was used throughout whole experiments. Copy paper (80 g m⁻²) was bought from Dongpo Paper. Craft paper (150 and 300 g m⁻²) was purchased from Shanghai ZiHao Trade Co., Ltd. Shape memory alloy (SMA) wires with a diameter of 0.5 mm were obtained from Lumenous Peiertech.

Synthesis of Ag FDs: The Ag FDs were obtained by the reduction of AgNO₃ by H₃NO at room temperature. Typically, 1.02 g of AgNO₃ and 1450 μL of H₃NO were dispersed in deionized water of 75 mL, respectively. The two solutions were uniformly mixed together by controlling the speed of the peristaltic pump to 30.0 rpm min⁻¹. The solutions were mixed in a three-necked flask and stirred continuously during the drop addition. The products were washed several times with deionized water and anhydrous ethanol, respectively.

Formulation of Ag FDs Conductive Ink: Conductive ink was obtained by mixing Ag FDs and SIS. First, 2.5 g of SIS was mixed with 20 mL of xylene which stirred at 600 rpm min⁻¹ for 720 min. Meanwhile, the wet Ag FDs were dried in a vacuum oven at 60 °C for 720 min. Then, 3.0 g of Ag FDs and 3.45 g of SIS solution were uniformly mixed to produce conductive ink.

Fabrication of the Ag FDs Paper-Based Heaters: Ag FDs paper-based heaters were fabricated by screen printing. The total length and width of the printing plate pattern were 288 and 50 mm, respectively. Heaters with specific patterns were printed on copy paper substrates using 300 mesh screens then dried at 80 °C for 30 min to remove xylene.

Preparation of OSA: A 300 g m⁻² craft paper cut to a shape, a length of 297 mm, and a width of 74 mm. Punched holes every 10 mm in the middle of the craft paper and through the SMA wire into the holes. At 7 mm on both sides of those holes, slots are cut in the lengthening direction. The copy paper cut into specific shape which keeps the same position as the slotting of the craft paper. The copy paper inserted the slot of the craft paper to complete the assembly. The whole folded according to the crease line.

Finite Element Method: We analyze the strain of different paper structures using the finite element method. The geometries of the flat structure and origami structures are constructed according to experimental structures. The material properties of all structures are considered as linear, elastic, and orthotropic, and their values are shown in **Table 1**. The x, y, and z directions are corresponding to the longitudinal, transverse, and normal directions of the paper sheet, respectively. The Young's moduli of the sheet in longitudinal and transverse directions are adopted from experimental measurements. The Young's moduli in the normal direction

Table 1. The material properties of the paper sheet used in FEM calculations.

Young's modulus [MPa]			Poisson's ratio			Shear modulus [MPa]		
E_x	E_y	E_z	ν_{xy}	ν_{yz}	ν_{zx}	G_{xy}	G_{yz}	G_{zx}
2500	1000	35[1]	0.34[1]	0.01[1]	0.01[1]	598	34	34

and the Poisson's ratios are taken from the literature.[34] The shear moduli (G) are derived by the following equations

$$G_{xy} = \frac{E_x E_y}{E_x + E_y(1 + 2\nu_{xy})} \tag{4}$$

$$G_{yz} = \frac{E_y E_z}{E_y + E_z(1 + 2\nu_{yz})} \tag{5}$$

$$G_{zx} = \frac{E_z E_x}{E_z + E_x(1 + 2\nu_{zx})} \tag{6}$$

where E is Young's modulus; ν represents Poisson's ratio.

The shell elements are used to discretize the domain considering the small thickness (0.384 mm) of the structures. The bottom end of the structures is fixed, and the force resulting from the deformation of the alloy wires is approximated and applied to the structure step by step till the vertical displacement of the top end achieves 60 mm. Given the large deformations of the structures, the geometric nonlinearity is included in the calculations. For origami structures, the thickness of the paper sheet is partially reduced to create the crease pattern. Modeling the origami creases is not a trivial task because the stiffness and strength along the crease can be lower than the facets due to fabrication.[27] Different methods have been implemented in the literature to model creases, one of which is to assign reduced mechanical properties to the elements near the creases.[27,35] As the stiffness on the crease is challenging to be experimentally measured, we reduce the thickness of the shell elements on the crease by 20% in our finite element model, leading to a reduction in the stiffness of the structure. As a comparison, the simulation is also performed without any reduction on the thickness of crease. It is shown in Figure S6 (Supporting Information) that the flexural rigidity of the 1:3 origami structure is slightly reduced if the thickness of the crease is decreased to 80% of the raw sheets, while both models predict quite similar mechanical behaviors.

Characterization: The structure characterization of Ag FDs and the crease of the heaters were observed with a field-emission SEM (Hitachi S-4800). XRD data was carried out on a X-ray diffraction (PANalytical X'Pert Pro, operating at 40 kV and 40 mA) with Cu Kα radiation ($\lambda = 0.15418$ nm). DSC data of SMA wires were recorded on DSC2-01118. Heating platform (Vectech V-3030T) provided stable temperature for SMA wires bending angle testing. The sheet resistance of heaters was measured with four-point probe resistance testers (FP-001). The heating effect of the heaters was monitored by an IR camera (FLIR ETS320). Temperature analysis of heaters was performed by the accompanying analysis software (FLIR Tools+). The folding test was completed on a motorized linear stage controlled by a DY-IS stepper motor controller, and monitor and record resistance changed using a Keithley-2400 digital multimeter.

Supporting Information

Supporting Information is available from the Wiley Online Library or from the author.

Acknowledgements

Conflict of Interest

The authors declare no conflict of interest.

Author Contributions

The design, preparation, and data analysis of OSA were completed by K.Z.; the characterizations of OSA were accomplished by K.Z., B.T., J.L., Q.L., and E.X.; mechanical behaviors of paper structures were carried out by Q.S., E.G., and K.Z.; K.Z. completed the first draft of the manuscript; W.W., E.G., Q.S., and J.L. have revised the manuscript; W.W. provided overall supervision of the work. All authors have approved the final manuscript.

Data Availability Statement

The data that support the findings of this study are available in the supplementary material of this article.

Keywords

[1] G. Li, X. Chen, F. Zhou, Y. Liang, Y. Xiao, X. Cao, Z. Zhang, M. Zhang, B. Wu, S. Yin, Y. Xu, H. Fan, Z. Chen, W. Song, W. Yang, B. Pan, J. Hou, W. Zou, S. He, X. Yang, G. Mao, Z. Jia, H. Zhou, T. Li, S. Qu, Z. Xu, Z. Huang, Y. Luo, T. Xie, J. Gu, et al., *Nature* **2021**, *591*, 66.

[2] C. Xin, D. Jin, Y. Hu, L. Yang, R. Li, L. Wang, Z. Ren, D. Wang, S. Ji, K. Hu, D. Pan, H. Wu, W. Zhu, Z. Shen, Y. Wang, J. Li, L. Zhang, D. Wu, J. Chu, *ACS Nano* **2021**, *15*, 18048.

[3] Y. Kim, G. A. Parada, S. Liu, X. Zhao, *Sci. Rob.* **2019**, *4*, eaax7329.

[4] S. M. Mirvakili, D. Sim, I. W. Hunter, R. Langer, *Sci. Rob.* **2020**, *5*, eaaz4239.

[5] Y. Tang, Y. Chi, J. Sun, T.-H. Huang, O. H. Maghsoudi, A. Spence, J. Zhao, H. Su, J. Yin, *Sci. Adv.* **2020**, *6*, eaaz6912.

[6] L. Miao, Y. Song, Z. Ren, C. Xu, J. Wan, H. Wang, H. Guo, Z. Xiang, M. Han, H. Zhang, *Adv. Mater.* **2021**, *33*, 2102691.

[7] F. Mushtaq, H. Torlakcik, M. Hoop, B. Jang, F. Carlson, T. Grunow, N. Läubli, A. Ferreira, X. Z. Chen, B. J. Nelson, S. Pané, *Adv. Funct. Mater.* **2019**, *29*, 1808135.

[8] F. A. Jerca, V. V. Jerca, R. Hoogenboom, *Chem* **2017**, *3*, 533.

[9] X. Wang, B. Yang, D. Tan, Q. Li, B. Song, Z. Wu, A. del Campo, M. Kappl, Z. Wang, S. N. Gorb, S. Liu, L. Xue, *Mater. Today* **2020**, *35*, 42.

[10] Y. Li, Z. Qi, J. Yang, M. Zhou, X. Zhang, W. Ling, Y. Zhang, Z. Wu, H. Wang, B. Ning, H. Xu, W. Huo, X. Huang, *Adv. Funct. Mater.* **2019**, *29*, 1904977.

[11] Y. C. Lai, J. Deng, R. Liu, Y. C. Hsiao, S. L. Zhang, W. Peng, H. M. Wu, X. Wang, Z. L. Wang, *Adv. Mater.* **2018**, *30*, 1801114.

[12] X. Hu, D. Zhang, S. S. Sheiko, *Adv. Mater.* **2018**, *30*, 1707461.

[13] C. Dingler, H. Muller, M. Wieland, D. Fauser, H. Steeb, S. Ludwigs, *Adv. Mater.* **2021**, *33*, 2007982.

[14] M. Pilz da Cunha, S. Ambergen, M. G. Debije, E. F. G. A. Homburg, J. M. J. den Toonder, A. P. H. J. Schenning, *Adv. Sci.* **2020**, *7*, 1902842.

ADVANCED
SCIENCE NEWS

www.advancedsciencenews.com

ADVANCED
INTELLIGENT
SYSTEMS
Open Access

www.advintellsyst.com

[15] Q. Ze, X. Kuang, S. Wu, J. Wong, S. M. Montgomery, R. Zhang, J. M. Kovitz, F. Yang, H. J. Qi, R. Zhao, *Adv. Mater.* **2020**, *32*, 1906657.

[16] H. T. Lee, M. S. Kim, G. Y. Lee, C. S. Kim, S. H. Ahn, *Small* **2018**, *14*, 1801023.

[17] Y. Park, X. Chen, *J. Mater. Chem. A* **2020**, *8*, 15227.

[18] B. Han, Y. Zhang, Q. Chen, H. Sun, *Adv. Funct. Mater.* **2018**, *28*, 1802235.

[19] Y. Xia, Y. He, F. Zhang, Y. Liu, J. Leng, *Adv. Mater.* **2021**, *33*, 2000713.

[20] K. Eschen, R. Granberry, B. Holschuh, J. Abel, *ACS Appl. Mater. Interfaces* **2020**, *12*, 54155.

[21] K. Hu, K. Rabenorosoa, M. Ouisse, *Front. Rob. AI* **2021**, *8*, 678486.

[22] X. Huang, K. Kumar, M. K. Jawed, A. M. Nasab, Z. Ye, W. Shan, C. Majidi, *Sci. Rob.* **2018**, *3*, eaau7557.

[23] H. T. Lee, F. Seichepine, G. Z. Yang, *Adv. Funct. Mater.* **2020**, *30*, 2002510.

[24] H. Rodrigue, W. Wang, M. W. Han, T. J. Y. Kim, S. H. Ahn, *Soft Rob.* **2017**, *4*, 3.

[25] M. M. Hamedi, V. E. Campbell, P. Rothemund, F. Güder, D. C. Christodouleas, J.-F. Bloch, G. M. Whitesides, *Adv. Funct. Mater.* **2016**, *26*, 2446.

[26] M. Axelsson, S. Svensson, *Pattern Anal. Appl.* **2009**, *13*, 159.

[27] S. Li, H. Fang, S. Sadeghi, P. Bhovad, K. W. Wang, *Adv. Mater.* **2019**, *31*, 1805282.

[28] B. G. Chen, B. Liu, A. A. Evans, J. Paulose, I. Cohen, V. Vitelli, C. D. Santangelo, *Phys. Rev. Lett.* **2016**, *116*, 135501.

[29] Y. Li, W. Liu, Y. Deng, W. Hong, H. Yu, *npj Flexible Electron.* **2021**, *5*, 3.

[30] Q. Liu, B. Tian, J. Liang, W. Wu, *Mater. Horiz.* **2021**, *8*, 1634.

[31] Q. Liu, B. Tian, C. Luo, J. Liang, W. Wu, *Adv. Mater. Technol.* **2020**, *5*, 2000278.

[32] L. Mao, Q. Meng, A. Ahmad, Z. Wei, *Adv. Energy Mater.* **2017**, *7*, 1700535.

[33] S.-I. Park, J.-H. Ahn, X. Feng, S. Wang, Y. Huang, J. A. Rogers, *Adv. Funct. Mater.* **2008**, *18*, 2673.

[34] Y. Xie, *Packag. Eng.* **2012**, *33*, 37.

[35] S. Fischer, *Int. J. Mech. Mater. Eng.* **2015**, *10*, 14.

Supporting Information

Modularized paper actuator based on shape memory alloy, printed heater, and origami

Ke Zheng[a], Enlai Gao[b], Bin Tian[a], Jing Liang[a], Qun Liu[a], Enbo Xue[a], Qian Shao[b]*,

and Wei Wu[a]*

[a] Laboratory of Printable Functional Materials and Printed Electronics, School of

Printing and Packaging, Wuhan University, Wuhan 430072, P. R. China.

[b] Department of Engineering Mechanics, School of Civil Engineering, Wuhan

University, Wuhan, 430072, P. R. China.

* Corresponding author:

qian.shao@whu.edu.cn (Q. Shao)

weiwu@whu.edu.cn (W. Wu)
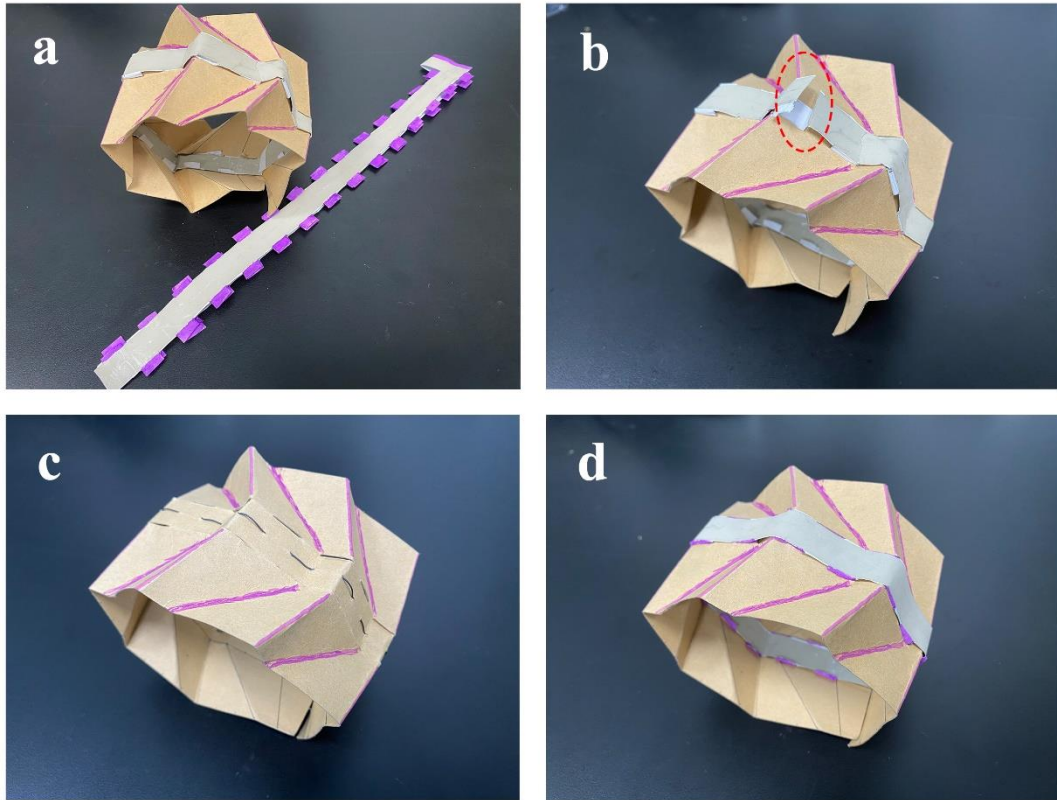
Figure S1. Components in OSA can be replaced. a) A normal origami actuator and a backup heater. b) Destroy OSA's heater. c) Remove OSA's heater. d) Install a backup heater for OSA.
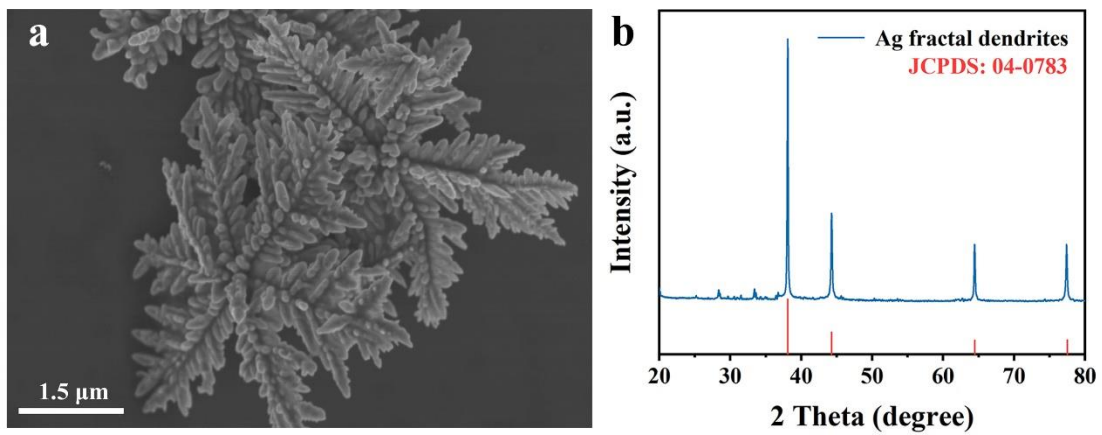

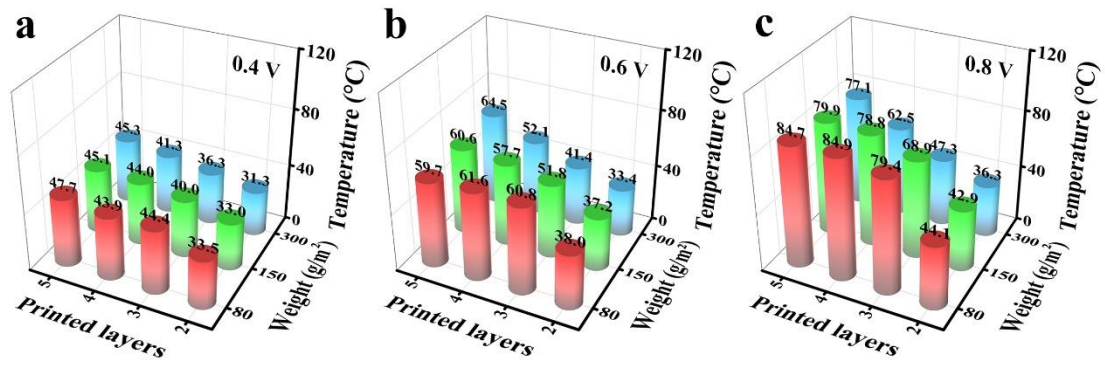**Figure S2.** a) SEM image of Ag FDs. b) XRD image of the Ag FDs.

Figure S3. The temperature at a) 0.4 V, b) 0.6 V, and c) 0.8 V apply to each of the 2, 3, 4 and 5 layers printed on H-80CoP, H-150CrP, and H-300CrP, respectively.
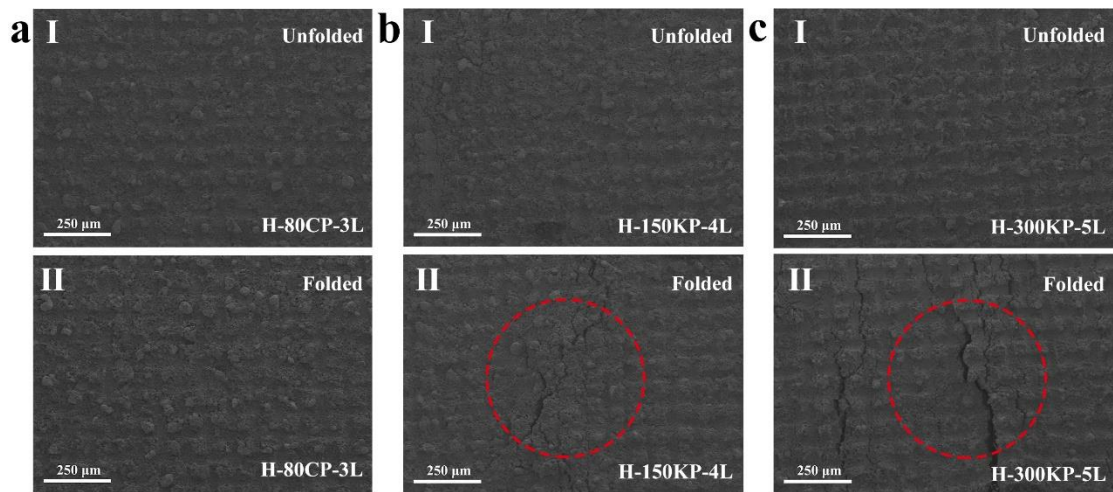

Figure S4. SEM images of a) H-80CP-3L, b) H-150kP-4L, and c) H-300kP-5L before and after folding.
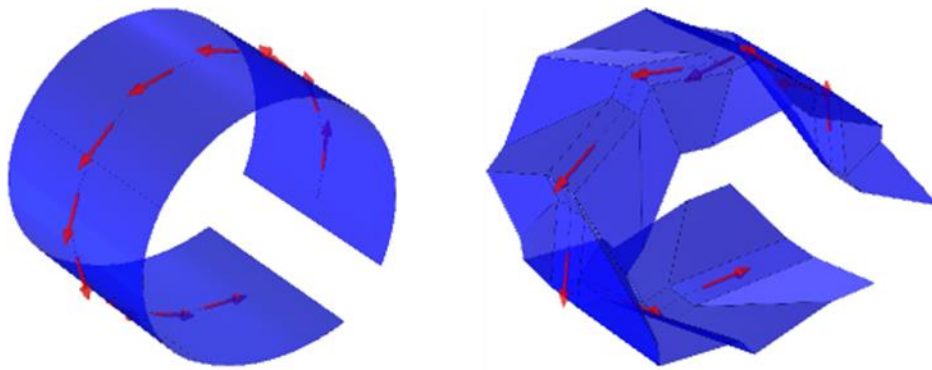

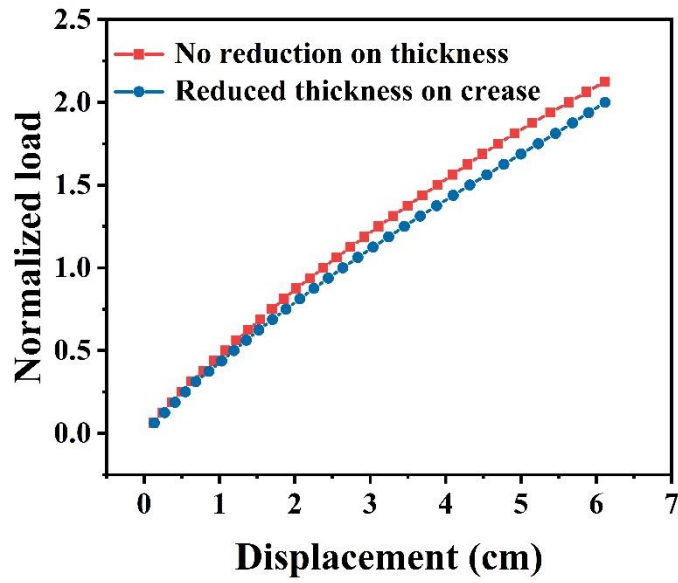**Figure S5.** Loads apply to the FSA and OSA in the FEM calculations.

Figure S6. The comparison of FEM predicted vertical displacement of the top end of the 1:3 origami structures with no reduction on thickness and a 20% reduction on thickness of crease.

Table S1. The parameters of the heaters are in the bending strain calculation

	h	$L_{initial}$	ΔL	r	ε
H-80CoP-3L	0.115 mm	26 mm	26 mm	4.14 mm	1.4%
H-150CrP-4L	0.216 mm	26 mm	26 mm	4.14 mm	2.6%
H-300CrP-5L	0.404 mm	26 mm	26 mm	4.14 mm	4.9%